Particle Accelerators, Vol. 63, pp. 105–137
Reprints available directly from the publisher
Photocopying permitted by license only

ELECTRON MULTIPACTING IN TESLA CAVITIES AND INPUT COUPLERS

PASI YLÄ-OIJALA*

Rolf Nevanlinna Institute, University of Helsinki, P.O. Box 4 (Yliopistonkatu 5), FIN-00014 Helsinki, Finland

(Received 8 January 1999; Revised 18 February 1999; In final form 8 March 1999)

Electron multipacting is a serious problem in many rf components operating in vacuum. The knowledge of the possible multipacting resonances is valuable when planning new rf designs and when struggling against multipacting in already existing structures. In this paper a detailed numerical analysis of electron multipacting in the TeV Energy Superconducting Linear Accelerator (TESLA) cavities and coaxial input couplers with ceramic windows is presented. TESLA is an international linear collider R&D effort based on superconducting components. The input coupler design for TESLA has been developed at both DESY and FNAL. In the couplers (both DESY and FNAL type) the discussion is confined to the cylindrically symmetric cold window sections. In the cavities the well-known (two-point) multipacting phenomenon is verified and the computed values agree with the measured ones. In the couplers the situation is more involved, since the rf operation conditions vary and a large number of simulations are required for a complete multipacting analysis. It is found that the cylindrical DESY window design is less sensitive to multipacting than the conical FNAL window design. With the present analysis method it is possible to optimize the rf operation conditions in the DESY design so that multipacting can be avoided.

Keywords: Multipacting; Superconducting cavities; Input couplers; Ceramic windows

1 INTRODUCTION

Multipacting is a phenomenon of resonant electron multiplication in which a large number of electrons build up an electron avalanche (see e.g. Ref. 1, Chapter 10). This avalanche can absorb the rf energy leading to remarkable power losses and heating of the walls. Multipacting can

* Fax: 358 9 19122779. E-mail: Pasi.Yla-Oijala@RNI.Helsinki.FI.

produce breakdown in high power rf components operating in vacuum, such as superconducting cavities, couplers and ceramic windows. This phenomenon starts if the following conditions are fulfilled:

1. An electron emitted from the cavity wall is driven by the electromagnetic field and returns back after an integer number of rf cycles to the same point of the cavity wall.
2. The impacting electron produces more than one secondary electron.

In the past multipacting was a major performance limitation in superconducting rf cavities. Therefore, in cavities multipacting has been studied by numerous authors.[2–5] Traditionally the multipacting calculations are based on straightforward Monte-Carlo type electron trajectory simulations. The most successful remedy to multipacting was the finding that in $\beta = v/c = 1$ cavities multipacting can be avoided by a proper choice of the cavity design.[4] However, multipacting is still a serious problem in many types of rf structures, such as low-β cavities, couplers, transmission lines and rf windows.

In the accelerator cavities multipacting can be completely analyzed by considering one or at most a couple of fundamental field modes. In input couplers the situation is more involved. During the operation of the rf pulse, i.e., while filling the rf cavity, the reflection conditions of the coupler vary and for a complete multipacting analysis a large number of simulations with various field conditions are required. Also the complexity of the coupler and window geometries increases the number of simulations. Especially, in the complicated 3D geometries a simulation of electron multipacting becomes very demanding. Thus, in order to analyze multipacting in input couplers with ceramic windows more advanced and efficient methods than a standard Monte-Carlo technique have to be developed.

In Ref. 6 we presented systematic computational methods to analyze multipacting in rf structures. The methods were based on traditional trajectory calculation combined with advanced searching and analyzing methods for multipacting resonances. The developed methods were applied in simple geometries, like straight and tapered coaxial lines, with various wave forms. Also the effect of biasing DC voltage to multipacting was studied in straight coaxial lines. In this article these methods are applied to analyze multipacting in TESLA[7] Test Facility (TTF)[8] superconducting cavities and power input couplers. We consider single

and multi-cell TTF cavities and the coaxial cold window geometries of both the Deutsches Elektronen-Synchrotron (DESY) and Fermi National Accelerator Laboratory (FNAL) input coupler designs with various reflection conditions. TTF is a linac prototype to the full-scale TESLA 500 GeV[7] design located at DESY and based on superconducting accelerator components. Since the geometries and the fields are axisymmetric, the trajectory calculation is two-dimensional. Figure 1 displays the geometries.

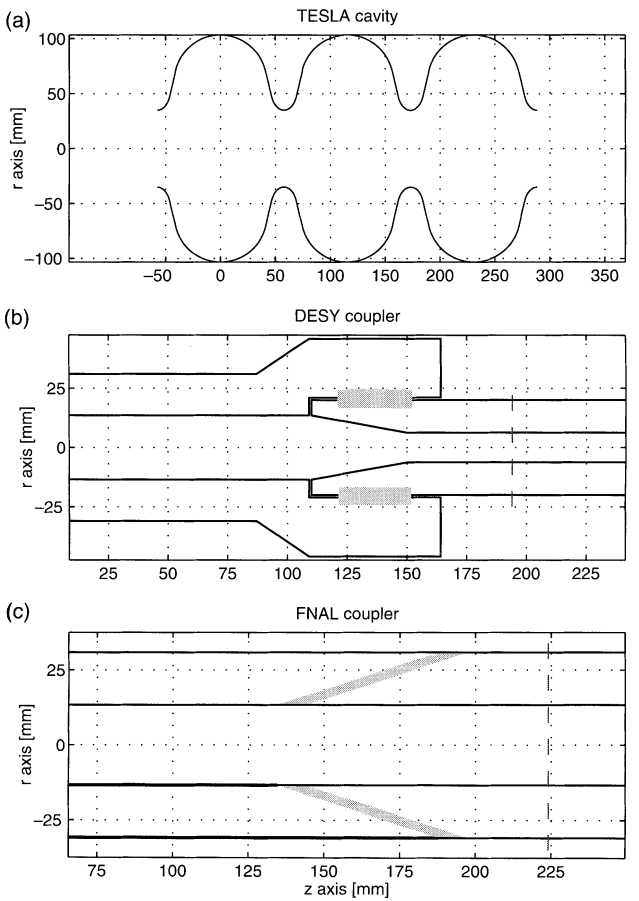

FIGURE 1 The cross-sections of the TESLA cavity (with 3 cells) (a) and the DESY (b) and FNAL (c) coaxial input coupler designs. The ceramic windows are denoted by shading. The vertical lines in (b) and (c) denote the reference planes where the reflection data are defined (see Section 4.1). The dimensions are in mm.

Multipacting might limit the performance of the input couplers. Therefore, it is very important for the input couplers to avoid such rf operation conditions which lead to multipacting. With the present analysis method we are able to find such operation conditions for the DESY coupler design which do not permit multipacting. In the FNAL coupler design multipacting appears on a wider range of operation conditions and additional methods, like the DC biasing voltage, are suggested to suppress multipacting. Together with our earlier results for coaxial lines[6,9,10] this article completes the study of multipacting phenomenon in the coaxial TTF couplers. However, the effect of DC voltage to multipacting in the window designs and multipacting in non-coaxial sections of the couplers, i.e., waveguide to coaxial transitions, are still open questions.

2 NUMERICAL METHODS

2.1 Field Computations

In multipacting the important phenomena related to the electron dynamics take place in the vicinity of the surfaces. Since multipacting is sensitive even to small perturbations of the rf field, the field computation near the structure walls needs special attention. Therefore, we have developed our own code for computing the electromagnetic fields. The code is based on the boundary integral equation method for solving Maxwell's equations and a special emphasis has been paid to the accuracy of the field computation near the boundaries. A detailed discussion of the method is given in Ref. 11. Furthermore, we have used other methods for the field computations. The finite element method (FEM) with a third order approximation[12] has been used for the field computation in the cavities and the finite volume element method[13] (FVEM) is applied for the field computation in the couplers with ceramic windows. A comparison of these three methods is presented in Ref. 11.

Since our field computing algorithms are able to treat closed domains only, the couplers, which in reality are open waveguides, are closed by properly placed electric walls. In straight homogeneous coaxial lines only the TEM-mode is propagating and mathematically we can set

electric walls to the zeros of the electric field. The positions of these "pseudo-walls" have to be chosen so that the reflected electromagnetic wave, generated by the nonhomogeneity, vanishes at the walls and the wave is settled down to the TEM-mode. Note that in rf cavities the pseudo-walls are not required, because the fundamental field mode is such that there are magnetic walls between the cavity cells. Furthermore, we require that the given frequency (here 1.3 GHz) is a resonant frequency of the resulting cavity. This gives the standing waves (SW) in a waveguide. By shifting the electric walls we may model several different SW field patterns in nonhomogeneous waveguides. The traveling waves (TW) and partially reflected waves (mixed waves, MW), needed for a complete multipacting analysis, can be obtained by appropriately combining two SW solutions as shown in the next section.

For the trajectory calculation the field values must be available in a grid. In other points the fields are evaluated by interpolation. In order to treat a huge number of trajectory calculations in the couplers with changing reflection conditions the field evaluation must be made as effective as possible. To this end, we do not directly use the field values at the grid points and interpolation elsewhere, but we calculate the coefficients $\alpha_0, \ldots, \alpha_3$ of a bi-linear interpolation (linear interpolation in both r and z directions) of the fields beforehand. For instance the radial component of the electric field is given at point (r, z) as

$$E_r(r, z) \approx \alpha_0^k + \alpha_1^k r + \alpha_2^k z + \alpha_3^k rz. \tag{1}$$

The coefficients $\alpha_j^k, j = 0, \ldots, 3$, are calculated and saved for each grid element $k = 1, 2, \ldots$ This simple idea makes the field evaluation more effective and speeds up the trajectory calculations by factor 10. Especially, this accelerating will be crucial for the 3D trajectory calculations.

2.2 Generating Mixed Waves

We call a purely traveling wave a *forward wave* if it propagates towards the cavity, and a traveling wave propagating away from the cavity, or reflected from the cavity, is called a *reflected wave*. The mixture of them with a complex reflection factor or coefficient R, $|R| \leq 1$, is called a *mixed wave*. The mixed waves in a straight coaxial line with TEM-mode

can be presented as follows:

$$\begin{aligned}\mathbf{E}(r,z,t) &= \mathrm{Re}\left(\frac{U}{r\ln(b/a)}(\mathrm{e}^{\mathrm{i}kz}+R\mathrm{e}^{-\mathrm{i}kz})\mathrm{e}^{-\mathrm{i}\omega t}\right)\mathbf{e}_r,\\ \mathbf{B}(r,z,t) &= \mathrm{Re}\left(\frac{U}{cr\ln(b/a)}(\mathrm{e}^{\mathrm{i}kz}-R\mathrm{e}^{-\mathrm{i}kz})\mathrm{e}^{-\mathrm{i}\omega t}\right)\mathbf{e}_\theta.\end{aligned} \tag{2}$$

Here Re stands for the real part of a complex number, (r,θ,z) are the cylindrical coordinates, t is time, c is the speed of light, U is the peak voltage between the conductors (for the forward wave), a and b are the inner and outer radii of the line, $\omega=2\pi f$, f is the frequency and $k=\omega/c$ is the wave number.

The magnitude of a complex reflection factor R describes the amplitude ratio of the reflected and forward waves, and the phase of R describes the phase difference of the reflected wave compared to the phase of the forward wave.

Next we show how mixed waves in nonhomogeneous waveguides (here coaxial lines with windows) can be obtained by combining two SWs. Let $\mathbf{E}_1$, $\mathbf{H}_1$ and $\mathbf{E}_2$, $\mathbf{H}_2$ denote SW fields with electric walls at $z=0, L_1$ and at $z=L_0, L_2$, respectively, so that the window lies clearly between L_0 and L_1, and $0<L_0<L_1<L_2$. Furthermore, we assume that the fields are in TEM-mode if $z\le L_0$ and $z\ge L_1$. We calibrate and normalize the fields so that $\mathbf{E}_1,\mathbf{H}_1$ and $\mathbf{E}_2,\mathbf{H}_2$ have the same peak voltage of 1 V. We are looking for a MW ($z\le L_0$ or $z\ge L_1$) with a given reflection coefficient R as a linear combination of the SW fields as follows:

$$\begin{aligned}\mathbf{E} &= \alpha_1\mathbf{E}_1+\alpha_2\mathbf{E}_2,\\ \mathbf{H} &= \alpha_1\mathbf{H}_1+\alpha_2\mathbf{H}_2,\end{aligned} \tag{3}$$

where α_1 and α_2 are complex constants, depending on R. By a straightforward calculation we get the following formulas for the coefficients

$$\begin{cases}\alpha_1 = U-\alpha_2\mathrm{e}^{-\mathrm{i}kL_0}\\ \alpha_2 = \dfrac{U(R-1)}{2\mathrm{i}\sin(kL_0)}.\end{cases} \tag{4}$$

Thus, by substituting (4) to (3) we get a MW (which is of the form (2)) with given voltage U and reflection coefficient R. In the numerical calculations we usually set $L_2 = L_1 + \lambda/4$, where λ is the wave length. In nonreflecting structures this gives $L_0 \approx \lambda/4$. The *forward power* of a MW is given by

$$P = \frac{U^2}{2Z}, \tag{5}$$

where Z is the line impedance. From (2) we see that the voltage of a MW is given by $U(1 + |R|)$. Thus, a SW has a voltage of 2U.

2.3 Methods to Analyze Multipacting

Next we give a short review of the computational methods used to analyze multipacting in rf structures.[6] Let us suppose that the field map is known and given in a sufficiently dense grid.

First, we send at a fixed field level a sufficiently large number of electrons from different points of the wall of the structure in different field phases. Let

$$p_0^{(j)} = (x_0^{(j)}, \varphi_0^{(j)}) \in \partial\Omega \times [0, 2\pi[; \quad j = 1, \ldots, N_0, \tag{6}$$

denote the initial sites. Here $\partial\Omega$ denotes the cavity wall. The initial velocity is assumed to be 2 eV and perpendicular to the wall. In reality the orientation of the initial velocity varies, but because electrons gain quickly energy much larger than a few eV, the variation of the initial velocity is usually not significant. Then the electron trajectories are computed by integrating the equations of motion of a relativistic electron and the place of the first impact on the wall x_1 together with the impact energy E_1 and corresponding field phase φ_1 are calculated. The trajectory calculation is continued up to a given number of impacts n, if at each impact the field phase is such that possible secondary electrons are able to leave the wall, i.e., if $\mathbf{E}(x_k, \varphi_k)$ points towards the surface for all $k \leq n$. Otherwise, the trajectory calculation is stopped.

At each impact $k = 1, 2, \ldots$, $\delta(x_k, E_k)$ new secondary electrons are emitted. For simplicity we assume that the *secondary yield function* δ only depends on the kinetic energy E_k of the impacted electron and

the material properties of the surface at the location of the impact x_k. The total number of secondary electrons due to a single electron launched at p_0 after n impacts is given by

$$N_n(p_0) = \prod_{k=1}^{n} \delta(x_k, E_k). \tag{7}$$

Obviously we set $N_n(p_0) = 0$ if the secondary electrons are not able to leave the wall after kth impact, $k \leq n$.

Figure 2 displays a typical secondary yield curve for a niobium surface.[14] For simplicity we assume that the secondary yield of all metallic surfaces (copper or niobium) and the ceramic window (usually made of aluminum oxide, Al_2O_3) is the same as for a niobium surface. In ceramic windows this assumption leads to modelling of the secondary yield of a coated ceramic (coated e.g. by a thin layer of titanium nitride, TiN) rather than the yield of a pure ceramic. A ceramic without a coating would have much higher secondary yield, the maximum yield being 2–9.[1] Naturally the results of the multipacting analysis depend strongly on the used secondary yield function.

After a given number of impacts (usually 20 or 30 impacts are computed), the number of secondary electrons is counted. This total number

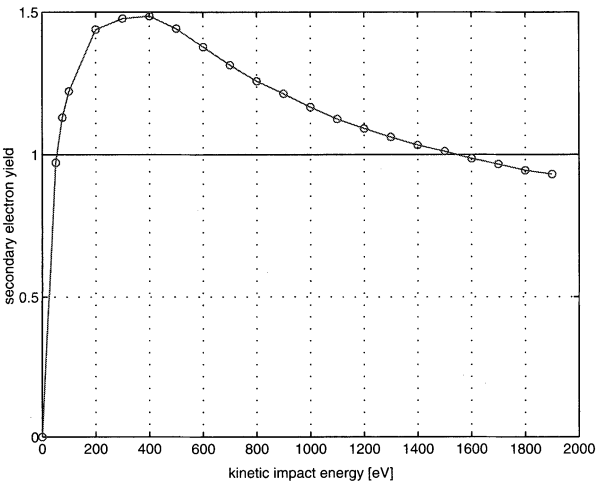

FIGURE 2 The secondary electron yield at different impact energies (in eV) for a niobium surface baked at 300°C.

of electrons is called an *enhanced counter function* and given by

$$e_n(|\mathbf{E}|) = \sum_{j=1}^{N_0} N_n(p_0^{(j)}). \tag{8}$$

We repeat the trajectory calculations with several fixed field levels. The scanning of the field levels $|\mathbf{E}|$ must be sufficiently dense to ensure that no multipacting resonances are missed. Obviously the enhanced counter function $e_n(|\mathbf{E}|)$ indicates whether the conditions for multipacting are fulfilled. More precisely, if for some field level $|\mathbf{E}|$ the number of electrons explodes, i.e.,

$$e_n(|\mathbf{E}|) \to \infty \quad \text{as } n \to \infty, \tag{9}$$

then multipacting is found. In the sequel, we study if the number of electrons is significantly increased in n impacts, i.e., whether the following condition is satisfied

$$\frac{e_n(|\mathbf{E}|)}{N_0} \gg 1 \tag{10}$$

for a sufficiently large n. The function e_n/N_0 is called a *relative enhanced counter function.*

3 MULTIPACTING IN CAVITIES

It has been found that in superconducting rf cavities multipacting can be overcome by changing the cavity shape from a cylindrical to a spherical or elliptical one.[4] In the spherical (and elliptical) cavities the fundamental accelerating field mode is such that the electrons will drift towards the cavity equator, eventually ending up to a region with very low electric field, where the impact energy is not high enough for a strong electron multiplication. This well-known phenomenon is clearly demonstrated here when we consider the single-cell TESLA 1.3 GHz cavity with the fundamental accelerating mode, TM_{010}-mode.

Typically an accelerating structure consists of a chain of coupled single-cell cavities. The TESLA superconducting cavities consist of 9 niobium cells. In the case of a multi-cell cavity the situation is however more involved. A chain of N coupled cells has N different eigenmodes with N different amplitude relations, if excited as a SW resonator.[1] Here

we consider the TESLA cavity with three cells. Figure 3 displays the electric field distributions along the axis of the TESLA three-cell cavity with so-called 0, $\pi/2$ and π-modes, according to the different amplitude relations.

In the following we study multipacting in two cases. Firstly, we consider the TM_{010}-mode in the single cell TESLA cavity. This corresponds to the π-mode in multi-cell cavities (all cells are excited to the same field level). Analysis of multipacting in this field configuration has been given in Ref. 15 some time ago and more recently in Refs. 16, 17. The multipacting resonances might depend on details of the cavity geometry. Therefore this calculation is repeated here for the TESLA cavity shape.

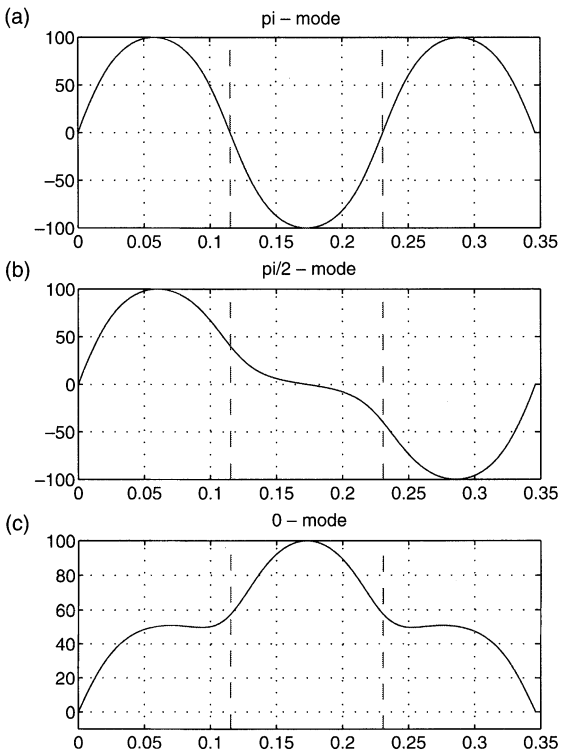

FIGURE 3 The electric field distributions due to $\pi, \pi/2$ and 0-modes along the axis of the TESLA cavity with three cells. The corresponding resonant (numerically determined) frequencies are 1.305, 1.298 and 1.285 GHz. The ends of the cells are denoted by vertical dashed lines.

Secondly, we consider the midmost cell of the three-cell TESLA cavity with the $\pi/2$-mode. This cell is often called an *empty* cell, because the electric field almost vanishes there (see Figure 3(b)). In the typical superconducting structure only the π-mode is used for acceleration. For diagnostic purpose the other resonances of the structure might be excited and a localization of a "bad" cell is possible because of the different excitation of the individual cells. Therefore one should know whether a new type of multipacting is possible in the field configuration of the so-called empty cell.

In the other cases, the outer cells of the $\pi/2$-mode and the 0-mode, the field distribution in the individual cells resembles the π-mode. Therefore in those cases multipacting phenomena may be reliable predicted by multipacting of the corresponding π-mode.

3.1 π-mode

First we consider the π-mode in the TESLA cavities. For the multipacting analysis we have sent 1620 electrons from the wall of the cavity in different field phases. Figure 4 shows the relative enhanced electron counter as a function of the accelerating field, E_{acc}, which is the time average of the electric field along the particles flight.[1] Figure 4 shows that the number of secondary electrons increases when E_{acc} is from 20 to 23 MV/m, i.e., when the electron counter exceeds the multipacting level $e_n(E_{\mathrm{acc}})/N_0 = 1$ (which in the 10 base logarithmic scale corresponds to 10^0).

Figure 5 displays electron trajectories when $E_{\mathrm{acc}} = 21$ MV/m. Figure 5(a) shows a long living trajectory drifting towards the cavity equator. Also the initial domain of those electrons which are clustered close to the cavity equator and start to repeat a resonant trajectory is denoted to the figure. This domain is rather large, $-45\ \mathrm{mm} \leq z \leq 45\ \mathrm{mm}$, where z is the z-coordinate of the initial point on the cavity wall. Furthermore, the trajectory calculations show that the order of the stable process close to the cavity equator is one, i.e., the flight time between successive impacts is one half rf cycle and the electron returns back to the initial point after one rf cycle.

However, the limit process possibly does not lead to multipacting, because the impact energy of the resonant electrons close to the cavity equator is rather low, merely about 70 eV. Figure 2 shows that the secondary yield exceeds one in the region 50–1500 eV. Thus, 70 eV is

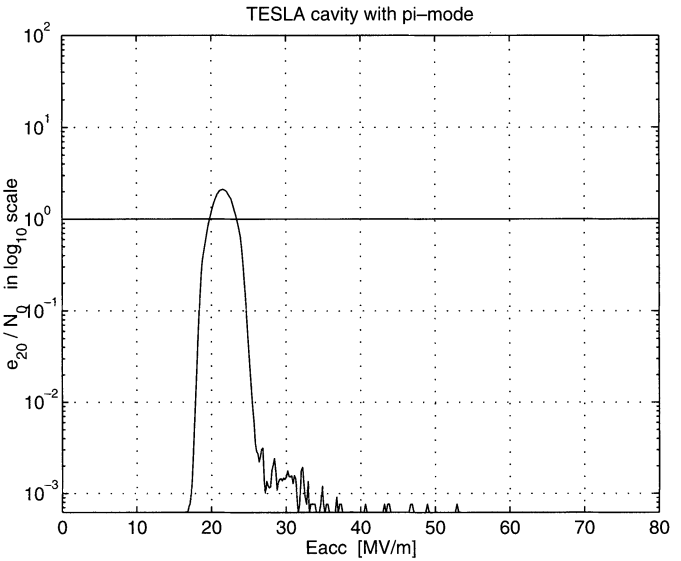

FIGURE 4 The relative enhanced electron counter in the 10 base logarithmic scale for the TESLA cavity with π-mode after 20 impacts. The horizontal axis gives the accelerating electric field in MV/m.

very close to the lower limit and whether this process corresponds to multipacting or not depends strongly on the secondary yield function. Figure 5(b) points out the regions where the impact energy is in the range 100–1500 eV. This is the case only on a narrow region around the cavity equator, roughly at $-4\,\text{mm} \leq z \leq -0.4\,\text{mm}$ and $0.4\,\text{mm} \leq z \leq 4\,\text{mm}$. The electron trajectory in Figure 5(b) will impact this region only three times.

The computed location and the field level of multipacting agree very well with the measurements made at DESY. The measured field level is from 17 to 22 MV/m.[18]

3.2 $\pi/2$-mode

Next we consider the midmost cell (empty cell) of the 3-cell TESLA cavity with $\pi/2$-mode. Figure 6 shows the relative enhanced counter function after 20 impacts. We are able to recognize one-point

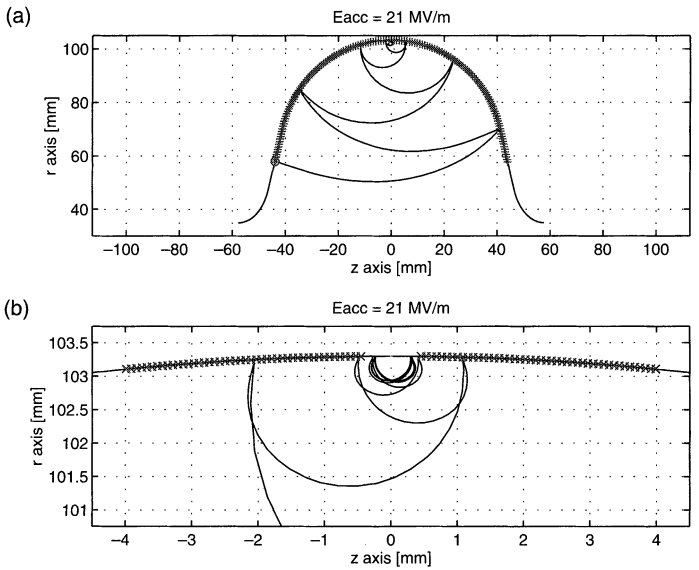

FIGURE 5 (a) Display of an electron trajectory in the TESLA cavity with π-mode when $E_{acc} = 21$ MV/m. The initial point is denoted by a circle (on the left hand side). The initial domain of those electrons which are drifted to the stationary trajectories close to the cavity equator is denoted by lineation. (b) Shows a zoomed plot close to the cavity equator. The region where the impact energy is in the range 100–1500 eV, i.e., the secondary yield is clearly larger than one, is indicated in (b).

multipacting of different order clearly outside the cavity equator (see Figure 7). Table I displays the multipacting field levels and rough approximations for the impact energies of the multipacting electrons. The (magnetic) field level is determined in the equator of the outermost cells where the field distribution resembles the π-mode. We see that only the processes of order 5, 6 and 7 may correspond to multipacting (the impact energy is in the range 50–1500 eV). However the counter function in Figure 6 suggests that none of the processes exceeds the multipacting-level $e_n/N_0 = 1$. This might be due to the facts that the number of electrons which start to multipact is very low compared to the number of initial electrons and the secondary electron yield is not strong enough for a large number of secondary electrons in 20 impacts. By focusing the analysis to the regions where the stationary trajectories take place or by computing more impacts, the counter in Figure 6 might show multipacting.

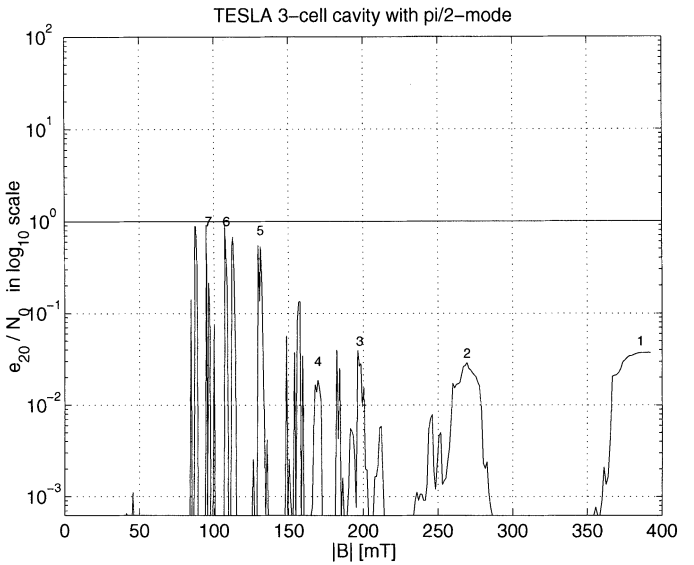

FIGURE 6 The relative enhanced electron counter for the empty cell of the 3-cell TESLA cavity with the $\pi/2$-mode in the 10 base logarithmic scale after 20 impacts. The horizontal axis gives the magnetic field in mT at the equator of the outer cells. The orders of the dominant processes are denoted to the plot. The other peaks correspond to the similar processes on the same region, which are, however, more instable.

TABLE I The magnetic field levels and impact energies of the one-point multipacting in the empty cell of the 3-cell TESLA cavity with the $\pi/2$-mode. The magnetic field is determined on the equator of the outer cells

Order	$\|\mathbf{B}\|$ (mT)	E_{kin} (eV)
7	95	840–850
6	110	1020–1040
5	129–130	1200–1230
4	165–169	2450–2450
3	195–201	2800–3500
2	255–280	4600–5600
1	360–425	6000–8000

Figure 7 shows the electron trajectories of the second and first order processes when $|\mathbf{B}| = 270$ and 380 mT, respectively. Multipacting occurs about 20–30 mm from the cavity equator and 75–95 mm from the axis.

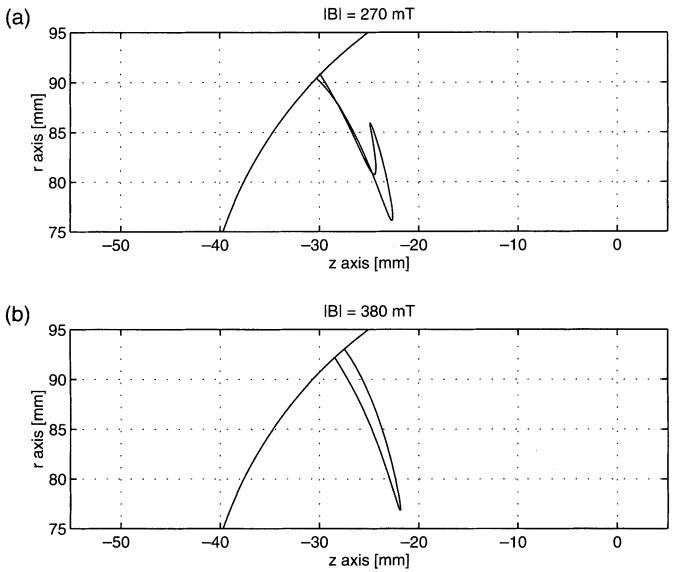

FIGURE 7 The electron trajectories in the empty cell of the 3-cell TESLA cavity with the $\pi/2$-mode when (a) $|\mathbf{B}| = 270$ (order 2) and (b) 380 mT (order 1). The equator of the empty cell is at $z = 0$.

4 MULTIPACTING IN INPUT COUPLERS

The input coupler design for TTF has been developed at both DESY and FNAL. Mean features of both designs include two vacuum windows, one cold (70 K) and one at room temperature, bellows on the inner and outer conductors of the coaxial line and a waveguide to coaxial transition. The part from the cold window to the cavity is called a *cold part* and the part from the cold window to the rectangular waveguide is called a *warm part*. More details about the configurations is given e.g. in Ref. 8. Here we investigate multipacting in the coaxial cold window sections of the couplers. The straight and tapered coaxial lines were treated in Ref. 6 and the bellows are neglected.

4.1 Reflection Conditions

During the operation of the rf pulse the reflection conditions on the coupler vary. Therefore, for a complete multipacting analysis we need

to know the amplitudes and phases of the reflected waves as functions of time. Figure 8 shows the reflection amplitudes and phases due to the DESY coupler design computed at DESY.[19] The data are computed for the cavity with no beam loading. In the case of a beam loading, which is switched on after about 800 μs, the reflected wave vanishes, because of an immediate match. Both cases, with and without the beam occur. Furthermore, in the ideal case the cavity is driven in resonance, but in practice the system is not ideally tuned. This leads to operation in the detuned state. The maximum detuning of ±10 degrees of the voltage phase compared to the driving signal can be assumed.

Since the time variation of R is very slow compared to the variation of the rf field (see Figure 8), the multipacting analysis may be carried out with several fixed reflection conditions. For each fixed R (about 100 altogether) the multipacting analysis is carried out as explained in Section 2.3 by sending several thousand electrons from the wall of the coupler, also from the surface of the window, but not from the straight

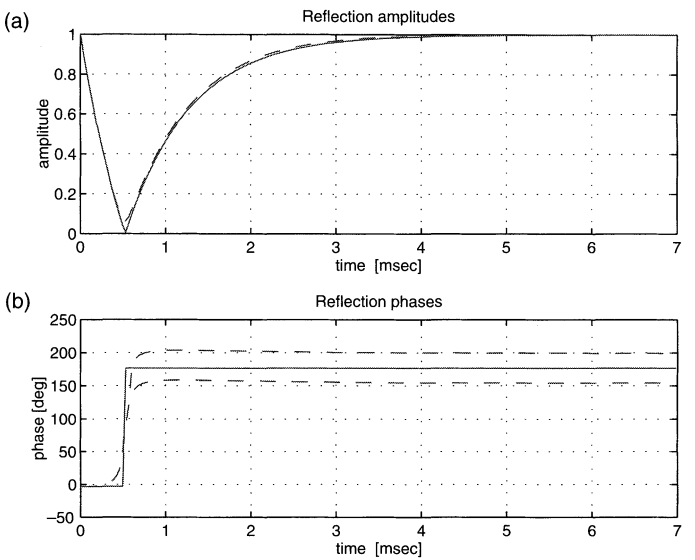

FIGURE 8 (a) Shows the reflection amplitudes as functions of time. In a similar fashion (b) gives the reflection phases. The reflection conditions denoted by a solid line correspond to the case when the cavity is operated at the resonance and the dashed lines correspond to the detuned operations.

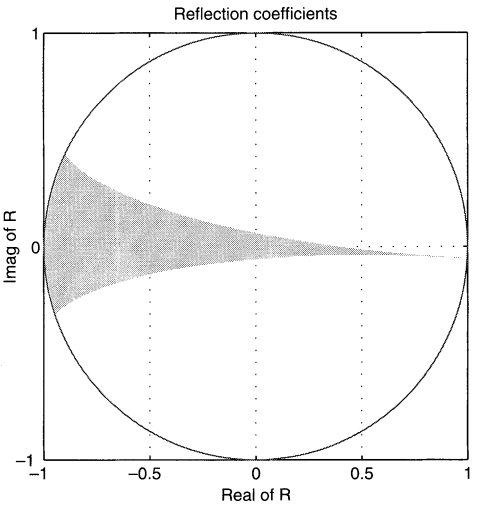

FIGURE 9 The complex reflection coefficients R for the DESY coupler. The shaded area shows the real operating range of the DESY coupler design ($t = 0$ on the right hand side, close to $R = 1$).

coaxial sections, in different field phases. Note that the results below do not include multipacting in the straight coaxial lines. We present the results of the multipacting analysis for all possible reflection conditions, i.e., for all complex R with $|R| \leq 1$. By using the data presented in Figure 9 one can read the possible multipacting regions from the figures below for the real reflection conditions.

4.2 DESY Input Coupler

First we consider the results of the multipacting analysis in the cylindrical DESY cold window design. The geometry is shown in Figure 1(b). The inner and outer radii of the coaxial line on the warm side are 13.5 and 31.0 mm, and the impedance is 50 Ω. On the cold side, on the other hand, the inner and outer radii of the coaxial line are 6.25 and 20.0 mm, and the impedance is 70 Ω. The frequency is 1.3 GHz.

The coordinate system is fixed so that $R = 1$ corresponds to a SW with a voltage maximum at the distance of one quarter wavelength from the center of the window. In Figure 1(b) this position is at $z = 194$ mm (denoted by a dashed line). This definition gives roughly a voltage

minimum to the center of the window and a voltage maximum to the antenna tip, i.e., to the center of the beam tube, at the beginning of the rf pulse. Eventually, at the end of the pulse (without the beam) the wave settles down to a SW, but the phase of the field is changed by 180 degrees (see Figure 8). Now there is a SW voltage maximum close to the center of the window. By a simple computing we find that changing the phase of the reflection coefficient, denoted by $\Delta\varphi$, corresponds to shifting the wave by

$$\Delta\varphi/(4\pi)\lambda. \tag{11}$$

Figures 10 and 11 show two-dimensional relative enhanced counters as functions of a complex reflection coefficient on the cold and warm

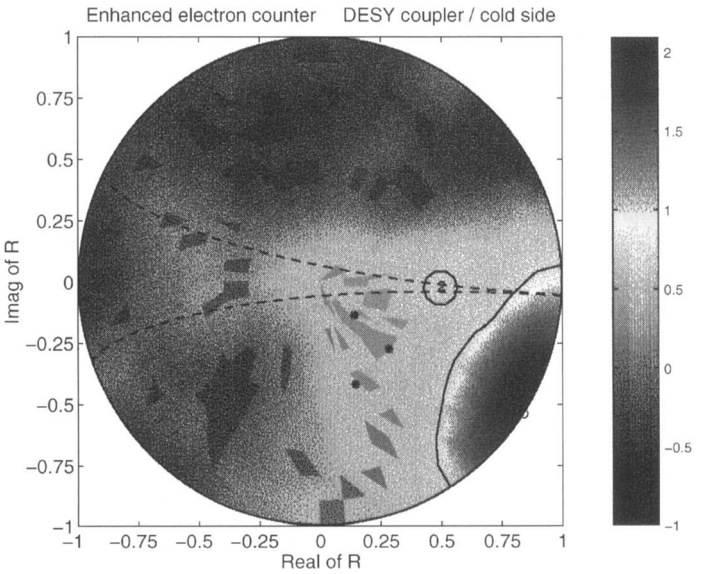

FIGURE 10 The relative enhanced electron counter for the cold side of the DESY coupler in 10 base logarithmic scale as a function of the complex reflection coefficient after 20 impacts. The real operation conditions are denoted to the plot by dashed lines (see Figure 9). The counter function shows multipacting on two separate regions, labeled by 1 and 2, corresponding to different types of multipacting. The circle ($R = 0.88 - 0.46i$) indicates the maximum of e_n. By stars we have denoted some discrete R values where multipacting is recognized but is difficult to identify. (See color plate I).

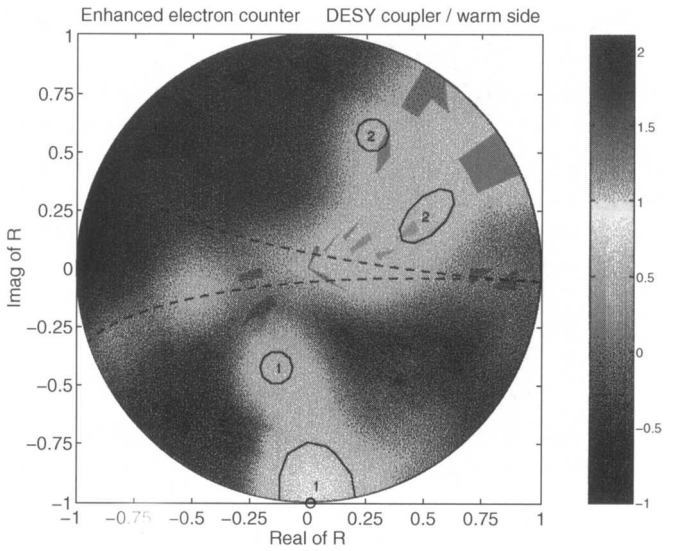

FIGURE 11 The relative enhanced electron counter for the warm side of the DESY coupler, in a similar fashion as in Figure 10. In this case multipacting occurs on four small separate regions, labeled by 1 and 2, corresponding to two different types of multipacting. The circle denotes the maximum of e_n ($R = -\mathrm{i}$). (See color plate II).

sides of the DESY design. In Figures 10 and 11 for each complex R we have plotted the maximum of the relative enhanced counter $e_n(P)/N_0$, $1 \leq P \leq 1000\,\mathrm{kW}$. Furthermore, the color indicates the change of the total number of electrons after 20 impacts. In red ($=2$) areas the number of electrons is increased by factor 100, whereas in dark blue ($=-1$) areas the number of electrons is decreased by factor 10. Hence, all positive values correspond to multipacting. The multipacting level $e_n(R)/N_0 = 1$ ($=0$ in logarithmic scale) is indicated by a solid line. By stars we have denoted some discrete R values where multipacting is recognized. We may conclude that on the cold side the dominating multipacting process takes place on the red region on the down-right of the reflection chart (region 1 in Figure 10), near the SW voltage minimum. On the warm side, on the other hand, the dominant multipacting takes place on two separate regions around $R = -\mathrm{i}$ and $R = -0.15 - 0.45\mathrm{i}$ (regions labeled by 1 in Figure 11).

Figures 12 (cold side) and 13 (warm side) display the enhanced electron counters as functions of the rf power and the corresponding

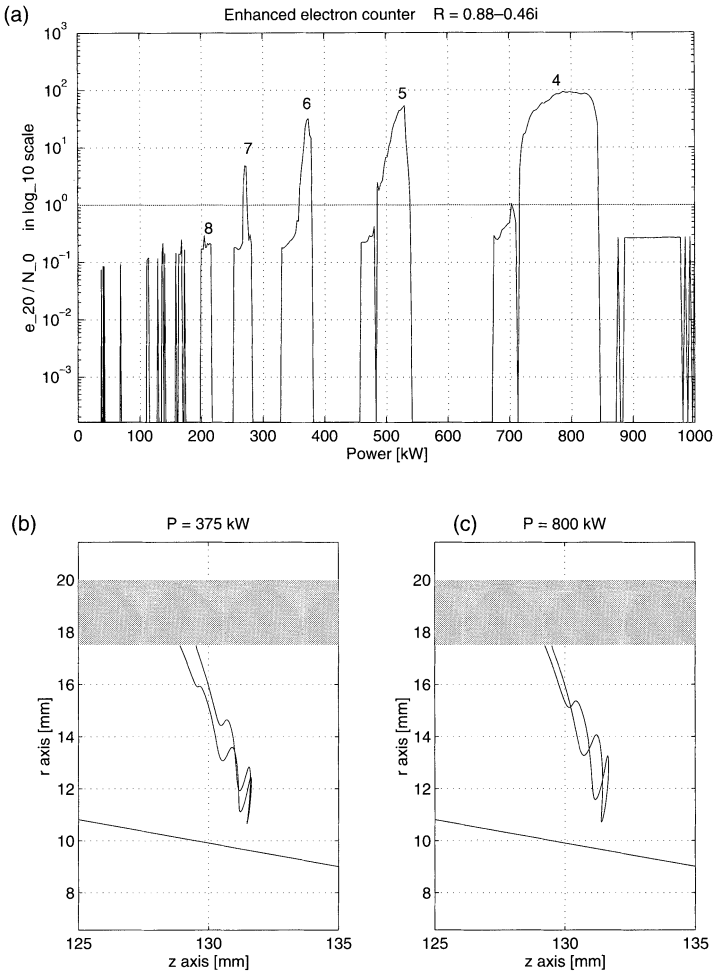

FIGURE 12 (a) shows a relative enhanced electron counter for the cold side of the DESY coupler in 10 base logarithmic scale as a function of the rf power when $R = 0.88 - 0.46\mathrm{i}$ (region 1 in Figure 10). The orders of the dominant processes are indicated in the figure. The broad peak at the right most, $870 \leq P \leq 990\,\mathrm{kW}$, corresponds to a two-point process of order one between the inner conductor and the window, close to the right end of the window. This process does not lead to multipacting, because the impact energy is too high. Same process appears on other R values, too (in suitable power levels leading to multipacting), but it is usually overlapping with the more prominent one-point multipacting; (b) and (c) give the multipacting electron trajectories when the rf power is 375 and 800 kW. The former process is of order 6 and the latter one is of order 4. The window is denoted by shading.

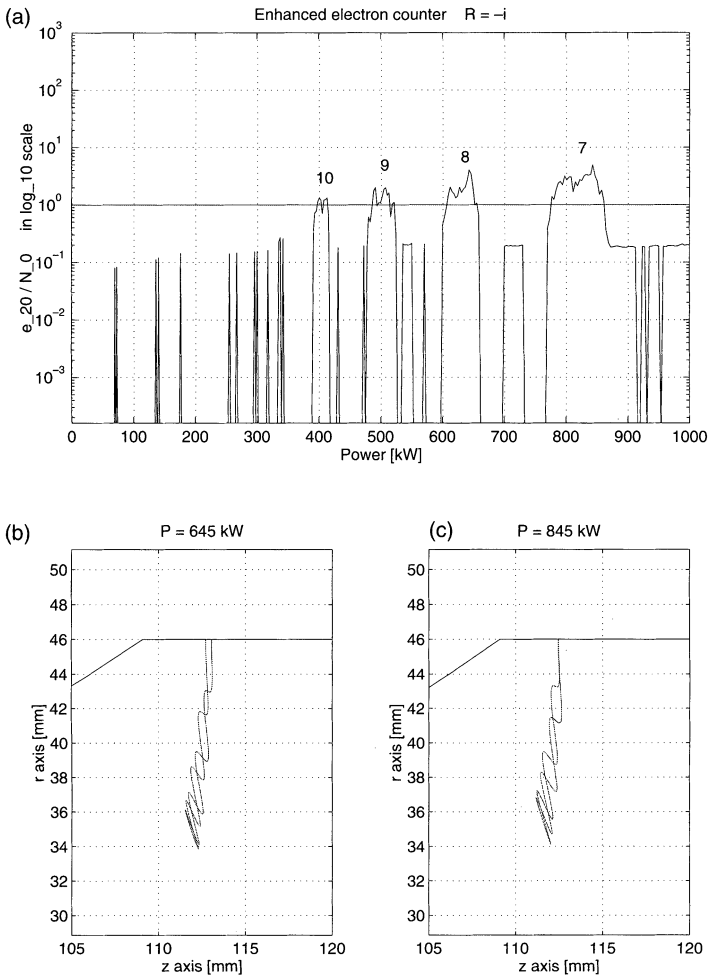

FIGURE 13 (a) Shows a relative enhanced electron counter for the warm side of the DESY coupler in 10 base logarithmic scale as a function of the rf power when $R = -\mathrm{i}$ (region 1 in Figure 11). The orders of the dominant processes are indicated in the plot; (b) and (c) show the multipacting electron trajectories when the rf power is 645 and 845 kW, respectively. The first one is of order 8 and the second one is of order 7.

multipacting electron trajectories when $R = 0.88 - 0.46\mathrm{i}$ and $-\mathrm{i}$, respectively. These R values are denoted by circles in Figures 10 and 11, and they correspond to the maxima of the enhanced counter. As the trajectories in Figure 12(b) and (c) show, on the cold side, there appear

one-point multipacting of different order on the inner surface of the window. Table II gives the multipacting power levels and the corresponding impact energies when $R = 0.88 - 0.46\,\mathrm{i}$. These multipacting power levels, however, shift as the reflection coefficient is changed. Furthermore, the trajectories in Figure 13(b) and (c) show that on the warm side one-point multipacting of different order takes place on the outer conductor.

Figure 14 illustrates the behavior of the multipacting processes due to the regions labeled by 2 in Figures 10 and 11. The trajectories due to the stars in Figure 10 are rather similar to the ones shown in Figure 14(c) (two-point multipacting between the window and the inner conductor). These processes are however more instable and therefore difficult to classify. To summarize we note that all multipacting processes which correspond to the regions labeled by 2, and by stars, take place on very narrow power regions and the secondary electron yield is rather low. Thus, in practice these processes are less harmful than the ones shown in Figures 12 and 13.

We may conclude that the condition for multipactor is fulfilled in relatively small areas in the reflection chart. One can avoid to operate in these dangerous areas by placing the window at the right distance from the coupler end. Unfortunately this is not done with the present design of the input coupler for TTF. The dashed lines in Figure 10 which denote the real operation conditions for the DESY design hit the dangerous area (at the beginning of the rf pulse). By rotating the operating area about 15 degrees counterclockwise, the multipacting area can be avoided. By (11) we find that this corresponds to shifting the window about 5 mm towards the generator.

TABLE II The rf power levels and impact energies of one-point multipacting on the cold side of the DESY coupler when $R = 0.88 - 0.46\mathrm{i}$

Order	P (kW)	E_{kin} (eV)
10	135–140	< 50
9	160–173	< 50
8	200–215	40–70
7	255–280	60–140
6	330–380	80–230
5	480–540	170–350
4	715–845	200–460

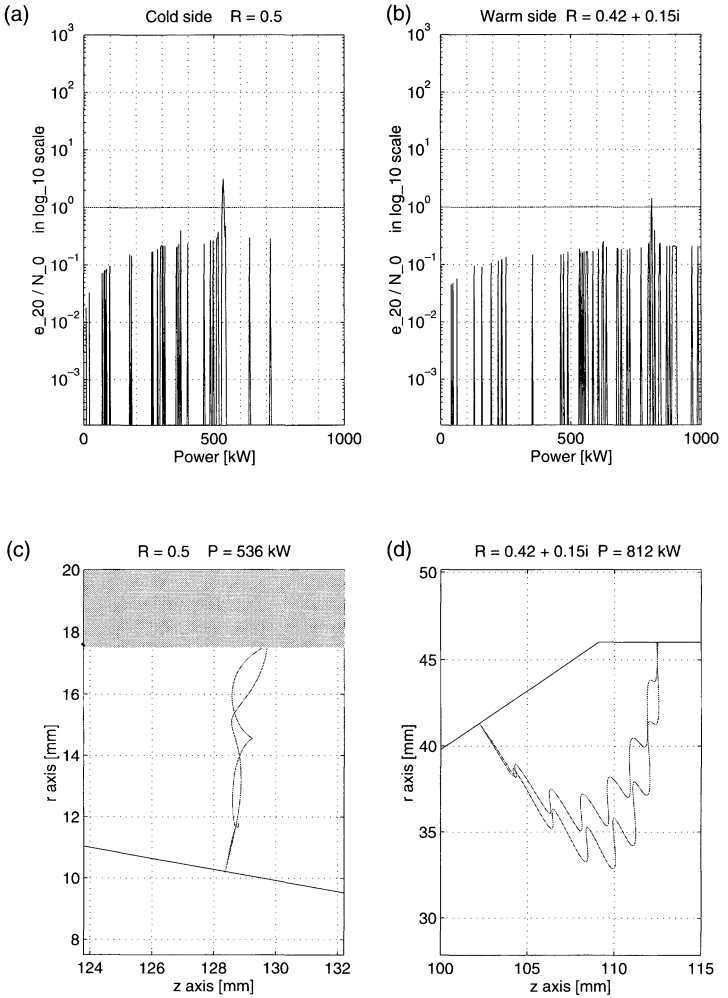

FIGURE 14 (a) Shows a relative enhanced electron counter for the cold side of the DESY coupler in 10 base logarithmic scale as a function of the rf power when $R=0.5$ (region 2 in Figure 10). (c) Shows the corresponding electron trajectory when the rf power is 536 kW. The order of the process is four. In a similar fashion, 14 (b) and (d) show a counter function and an electron trajectory on the warm side of the DESY coupler when $R=0.42+0.15\mathrm{i}$ (region 2 in Figure 11) and $P=812$ kW. The order of this two-point multipacting is 14.

4.3 FNAL Input Coupler

Next we consider the multipacting analysis of the FNAL conical cold window design without the tapering. The geometry is shown in Figure 1(c). The inner and outer radii of the coaxial line are 13.34 and 30.86 mm, and the impedance is 50 Ω. The frequency is 1.3 GHz. Our geometry is slightly modified version of the real geometry. We have neglected some details on the junctions of the window and the conductors. Our experiments show that these modifications (and the missing tapering) do not significantly affect the found multipacting phenomenon, which is predominantly due to the conical shape of the window.

The coordinate system is again fixed so that $R = 1$ corresponds to a SW with a voltage maximum at the distance of one quarter wavelength from the center of the window. In Figure 1(c) this position is at $z = 224$ mm (denoted by a dashed line).

Figures 15 and 16 show two-dimensional enhanced electron counters for the FNAL window design in a similar fashion as for the DESY design above. On the cold side we are able to recognize three discrete

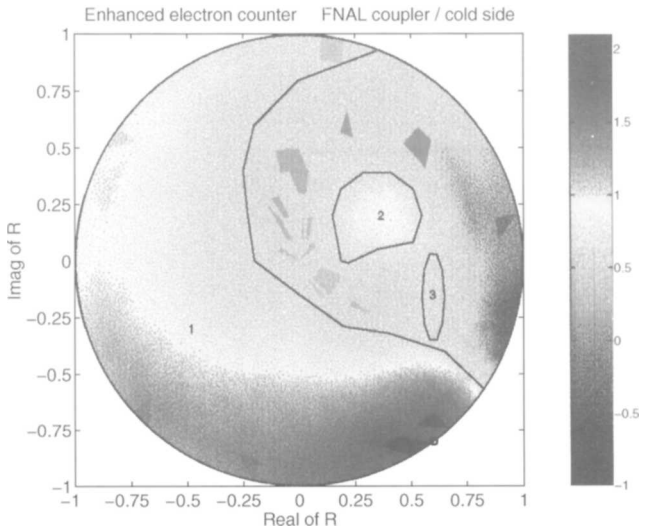

FIGURE 15 The relative enhanced electron counter for the cold side of the FNAL coupler in 10 base logarithmic scale, in a similar fashion as for the DESY coupler above. The counter function shows three discrete multipacting regions (indicated by lines and labeled by 1, 2 and 3). The maximum of the counter function e_n is denoted by a circle, that is, $R = 0.6 - 0.8i$. (See color plate III).

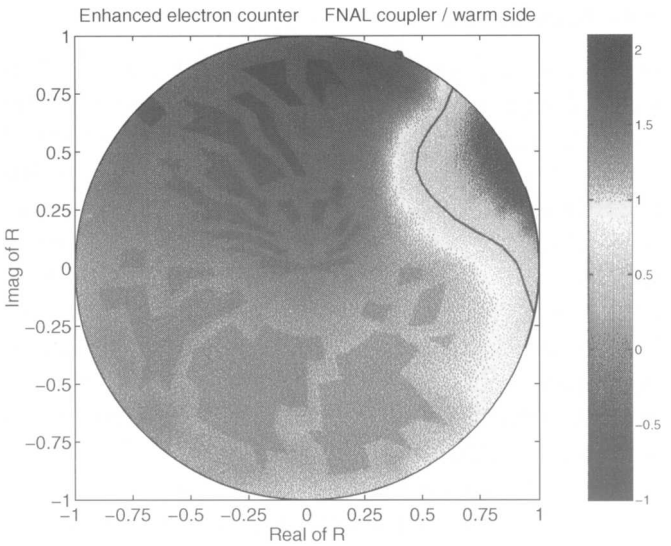

FIGURE 16 The relative enhanced electron counter for the warm side of the FNAL coupler. The counter function shows that multipacting occurs on almost everywhere on the reflection chart. There is a rather small blue area on the top-right where multipacting is not found. The maximum of the counter function e_n is denoted by a circle ($R = 0.40 + 0.91$i). (See color plate IV).

multipacting regions, a large area on the left hand side (labeled by 1) and two smaller regions near $R = 0.35 + 0.2$i (labeled by 2) and $R = 0.6 - 0.15$i (labeled by 3). On the warm side the counter function shows multipacting on a very large region on the reflection chart.

Figure 17 shows relative enhanced counters on the cold side as functions of the rf power when $R = -1$ (SW with the voltage maximum in the middle of the window) and $R = 0.60 - 0.80$i (the maximum of $e_n(R)$) and the corresponding multipacting electron trajectories. The trajectories show that there exists two-point multipacting of order one between the inner conductor and the (inner) surface of the window close to the junction of the window and the inner conductor. We have also found higher order one-point and two-point multipacting (regions 2 and 3 in Figure 15). Figure 18 displays trajectories when $R = 0.2$ and $R = 0.6$. These higher order processes appear on very narrow power regions and are in practice less significant than the dominating multipacting process which is illustrated in Figure 17 (and in Figure 19). Note that in the TW case, $R = 0$, all electrons are drifting away from the window region in 20

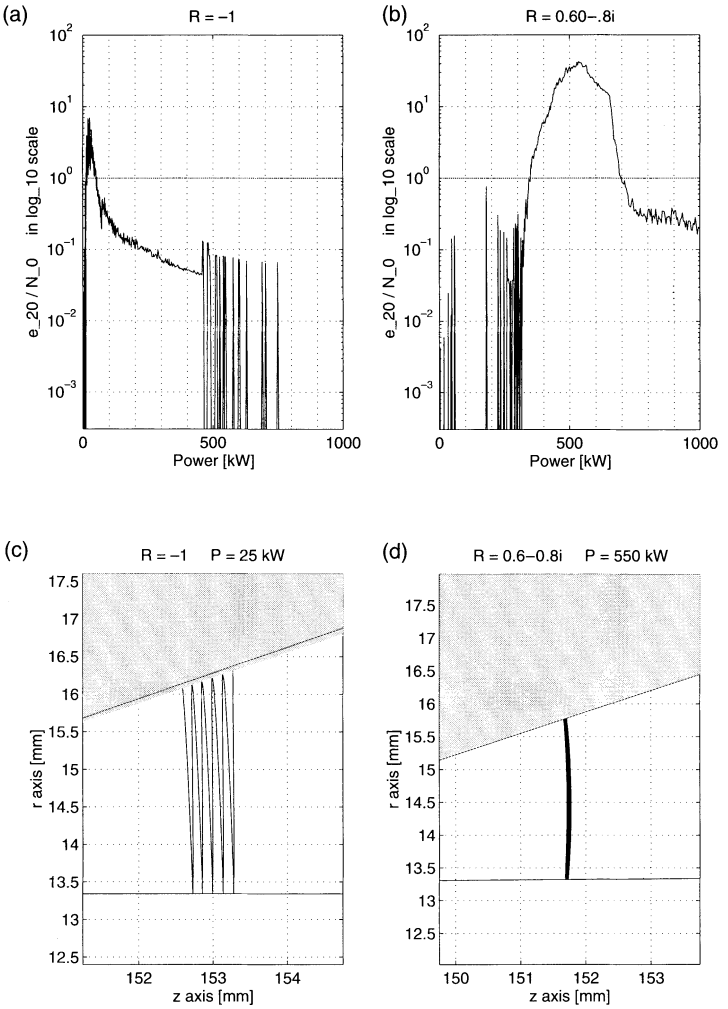

FIGURE 17 (a) and (b) give relative enhanced electron counters for the cold side of the FNAL coupler in 10 base logarithmic scale when $R=-1$ and $R=0.6-0.8\mathrm{i}$ (in region 1 in Figure 15); (c) and (d) show the multipacting trajectories (10 impacts) when $P=25\,\mathrm{kW}$, and $P=550\,\mathrm{kW}$, respectively. In both cases the order of multipacting is one. The window is denoted by shading.

impacts. Thus, in the TW operation multipacting may occur only on the warm side.

In a similar fashion, Figure 19 shows relative enhanced counters on the warm side when $R=-1$, $R=0$ (TW) and $R=0.40+0.91\mathrm{i}$

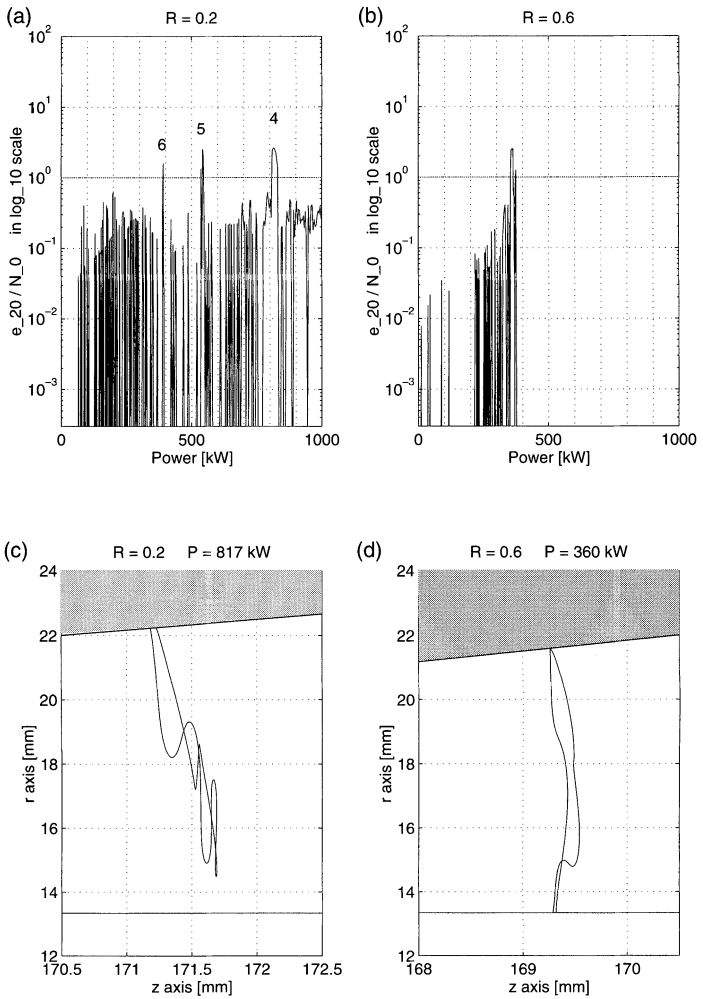

FIGURE 18 (a) and (b) give relative enhanced electron counters for the cold side of the FNAL coupler in 10 base logarithmic scale when $R = 0.2$ (region 2 in Figure 15) and $R = 0.6$ (region 3 in Figure 15); (c) and (d) (not into scale) show the corresponding electron trajectories when $P = 817\,\text{kW}$, and $P = 360\,\text{kW}$, respectively. In both cases the order is four (the orders are indicated in (a)).

(the maximum of $e_n(R)$), and the corresponding multipacting electron trajectories. Now there exists two-point multipacting of order one between the outer conductor and the (outer) surface of the window close to the junction of the window and outer conductor. Figure 19(c)

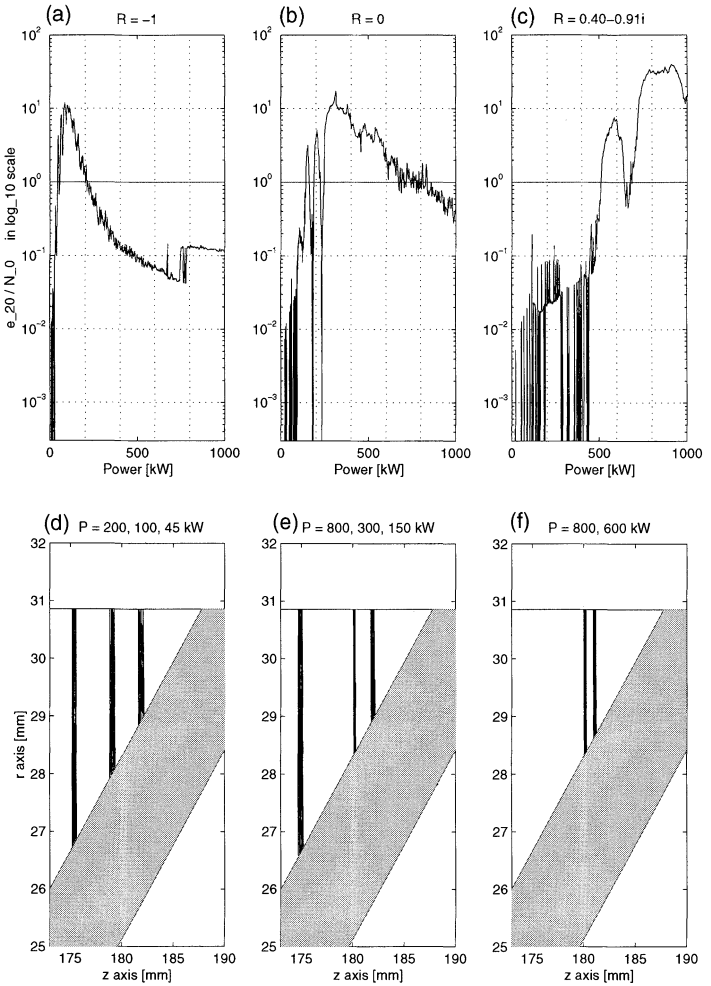

FIGURE 19 (a), (b) and (c) give the relative enhanced electron counters as functions of the rf power for the warm side of the FNAL coupler in 10 base logarithmic scale when $R=-1$, 0 and $0.40+0.91i$; (d), (e) and (f) (10 impacts, not into scale) show the corresponding multipacting trajectories (first order) when $P=200$, 100 and 45 kW (in (d)), 800, 300 and 150 kW (in (e)), and 800 and 600 kW (in (f)), from left to right.

suggests that there is no multipacting when $P \approx 650$ kW. From the trajectories displayed in Figure 19(f) we can, however, conclude that this is due to a finite discretization and Figure 19(c) should show a continuous multipacting barrier above 500 kW. Figure 19(d)–(f) shows

also that the multipacting electrons glide along the surface of the window from right to left as the rf power is increased. This explains the broadness of the multipacting power bands in Figure 19(a)–(c). Actually, the multipacting process finds a suitable "gap distance" (distance between the window and the conductor) and rf power combination. Hence, the location and power level of multipacting are strongly related to the field pattern. This relation is studied more carefully in Figure 20. Similar phenomenon is found on the cold side, too.

On the warm side we were not able to recognize one-point multipacting. However, the one-point and higher order two-point processes may be overlapped with the dominating two-point multipacting.

Figure 20 displays the multipacting power levels on the warm side as the reflection coefficient is varied. Close to the zero phase of R, i.e., when there is a voltage minimum near the center of the window, the multipacting power levels either disappear or move to very high power levels ($P > 1000\,\text{kW}$). Furthermore, from the shapes of the electron trajectories and from the fact that multipacting occurs at the SW voltage maximum, we may conclude that multipacting in the FNAL window design is predominantly due to the electric field. (In the DESY design the electron trajectories are typical multipacting trajectories in the region of a high magnetic field, thus the shapes of the trajectories are predominantly due to the magnetic field.) However, in both cases, on the cold and warm sides of the FNAL design, the maximum of $e_n(R)$ is attained when the SW electric field minimum is (roughly) at the junction of the window and the inner (cold side) or outer (warm side) conductor. Thus, in those cases multipacting appears near the magnetic field maximum ("two-point magnetic multipacting"). The corresponding trajectories are displayed in Figures 17(d) and 19(f). The trajectories show that in those cases multipacting is more stable and more focused than in the other cases shown above.

While writing this paper, the real reflection conditions for the FNAL coupler were not available, but they might be rather similar as the DESY data which are given above. In both designs the window is placed so that there is a SW voltage minimum on the window region at the beginning of the rf pulse. On the other hand, as Figures 15 and 16 show, multipacting appears on so broad region on the reflection chart that it is impossible to find such realistic reflection conditions in the FNAL design which do not lead to multipacting.

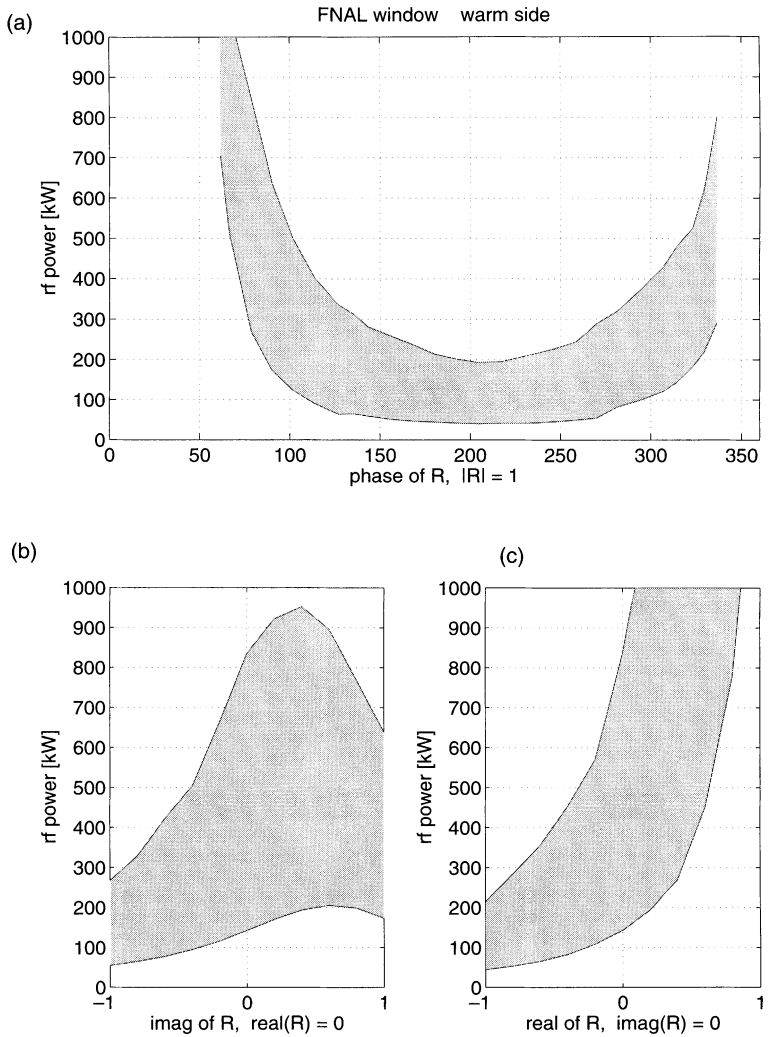

FIGURE 20 The multipacting power levels on the warm side of the FNAL conical window are plotted as a function of the reflection coefficient. (a) shows the multipacting power levels as the phase of the complex reflection coefficient R with $|R| = 1$ is varied, i.e., the multipacting power levels for various SW field patterns. (b) and (c) show the multipacting power levels when the magnitude of R is varied. In (b) $\mathrm{Re}(R) = 0$ and in (c) $\mathrm{Im}(R) = 0$. The shaded areas correspond to the power regions where the relative enhanced counter exceeds one. Note that the process usually exists on the higher power levels too, above the shaded area, but the impact energy is too high for multipacting. These graphs correspond to Figure 16 as follows. Figure (a) corresponds to moving along a ring $|R| = 1$, (b) corresponds to moving along a vertical line from $-i$ to i and (c) corresponds to moving along a horizontal line from -1 to 1, respectively.

5 CONCLUSIONS

In this work the computational methods developed in Ref. 6 are applied to analyze electron multipacting in the TESLA superconducting cavities and power input couplers. We have considered single-cell cavities and three-cell cavities with 0, $\pi/2$ and π-modes. In the input couplers the multipacting analysis is carried out on the cylindrically symmetric cold window sections. Both the DESY and FNAL window designs are considered.

In the TESLA cavity with the π-mode the well-known two-point multipacting of order one close to the cavity equator is recognized. In the $\pi/2$-mode we have found one-point multipacting of different order on a narrow region clearly outside the equator of the midmost cell (so-called empty cell). In both cases, however, the secondary electron yield is rather low.

The numerical simulations show that the DESY coupler design with a cylindrical window is less sensitive to multipacting than the FNAL coupler design with a conical window. In the DESY design the conditions for multipacting are fulfilled in small separate regions on the reflection chart. The dominating multipacting process is one-point multipacting of different order on the inner surface of the window close to the SW voltage minimum. In particular, one can avoid to operate in these dangerous areas by placing the window at the right distance from the coupler end. In the FNAL design this is not possible because of a much wider existence of multipacting. The analysis shows two-point multipacting of order one between the conductors and the surface of the window on both sides of the window. In this case the conditions for multipacting are fulfilled almost everywhere but not at the SW voltage minimum.

Because of the complexity of the window geometries and of varying field conditions during the operation of the system a lot of simulations are required in order to reliably predict multipacting in the input couplers. In this work these resonances are located and identified in two special designs. On the other hand the complex geometry of input couplers and ceramic windows makes it difficult (in many cases even impossible) to give any general rules for multipacting. Therefore, in each new design the multipacting resonances need to be recalculated.

Acknowledgments

Part of the multipacting analysis and field computations in the input couplers are carried out by M. Ukkola and H. Mäkiö at Rolf Nevanlinna Institute. The reflection data for the DESY coupler and part of the cavity fields are calculated at DESY by B. Dwersteg and J. Sekutowicz. They all are greatly acknowledged. Moreover, the author wish to thank D. Proch from DESY for a very pleasant and fruitful co-operation, and for reading the manuscript. This work was supported by financial help of DESY.

References

[1] H. Padamsee, J. Knobloch and T. Hays. *RF Superconductivity for Accelerators*, John Wiley & Sons, inc., New York, 1998.
[2] I. Ben-Zvi, J.F. Crawford and J.P. Turneaure. Electron multipacting in cavities, *IEEE Trans. Nuclear Science*, **20**, 54 (1973).
[3] C.M. Lyneis, H.A. Schwettman and J.P. Turneaure. Elimination of electron multipacting in superconducting structures for electron accelerators. *Appl. Phys. Lett.*, **31**, 541 (1977).
[4] U. Klein and D. Proch. Multipacting in superconducting RF structures. *Proceedings of the Conference on Future Possibilities for Electron Accelerators*, Volume N1-17, Charlottesville (1979).
[5] R. Boni, V. Chimenti, P. Fernandes, R. Parodi, B. Spataro and F. Tazzioli. Reduction of multipacting in an accelerator cavity, *IEEE Trans. Nuclear Science*, **32**, 2815 (1985).
[6] E. Somersalo, P. Ylä-Oijala, D. Proch and J. Sarvas. Computational methods for analyzing electron multipacting in RF structures, *Particle Accelerators*, **59**, 107 (1998).
[7] R. Brinkmann, G. Materlik, J. Rossbach and A. Wagner. Conceptual design of a 500 GeV e^+e^- linear collider with integrated X-ray laser facility, Volume I, DESY 1997-048, ECFA 1997-182, 1997.
[8] D.A. Edwards (Ed.). TESLA Test Facility linac – Design report, TESLA Reports 95-01, DESY Print 1995.
[9] P. Ylä-Oijala. Analysis of electron multipacting in coaxial lines with traveling and mixed waves. TESLA Reports 97-20, 1997.
[10] P. Ylä-Oijala. Suppressing electron multipacting in coaxial lines by DC voltage. TESLA Reports 97-21, 1997.
[11] P. Ylä-Oijala and E. Somersalo. Computation of electromagnetic fields in axisymmetric RF structures with boundary integral equations, *Journal of Electromagnetic Waves and Applications*, **13**, 445 (1999).
[12] J. Sekutowicz. 2D FEM code with third order approximation for RF cavity computation, *Proceedings of Linear Accelerators Conference in Tsukuba* Japan (1994).
[13] H. Mäkiö. A finite volume element method for electromagnetic field computations of RF-resonators, *Pitman Research Notes in Mathematics: Integral Methods in Science and Engineering, Vol. 2: Approximation Methods*, Longman 1997.
[14] R. Calder *et al. Nucl. Instrum. Methods Phys. Res. B, Beam Interact. Matter. At.*, **13**, 631 (1986).

[15] W. Weingarten. Electron loading, *Proceedings of the 2nd Workshop on RF Superconductivity*, edited by H. Lengeler, CERN, Geneva, Switzerland, 551 (1984).
[16] J. Knobloch, W. Hartung and H. Padamsee. Multipacting in 1.5-GHz superconducting niobium cavities of the CEBAF shape, *8th Workshop on RF Superconductivity*, Padova, Italy (1997) (SRF 981012-09, Cornell Report).
[17] J. Knobloch. Advanced thermometry studies of superconducting radio-frequency cavities, Ph.D. Thesis, Cornell University, CLNS 97-3, 1997.
[18] D. Proch, Personal communication, DESY, 1998.
[19] B. Dwersteg, Personal communication, DESY, 1998.